



Cite this: *RSC Adv.*, 2025, 15, 30782

The electronic structure, optical, and thermoelectric properties of novel Bi_2PbCh_4 (Ch = Se, Te) materials: insights from first-principles study

Mohannad Mahmoud Ali Al-Hmoud,^a Banat Gul,^b Muhammad Salman Khan,^c *^{cd} Siti Maisarah Aziz,^d Zia Ullah,^e Ghlamallah Benabdellah^e and Ayed M. Binzowaimil^a

Ternary chalcogenides have attracted much interest because of their potential for use in sustainable energy applications due to their tunable electronic, optical, and transport characteristics. This work examined the structural, electronic, optoelectronic, and thermoelectric properties of novel Bi_2PbSe_4 and Bi_2PbTe_4 chalcogenides through density functional theory. The predicted energy gap values measured with the TB-mBJ and PBE-GGA are 1.12 and 0.71 eV for Bi_2PbSe_4 and 1.08 and 0.82 eV for Bi_2PbTe_4 , respectively. Both materials behave as semiconductors and have direct energy gaps, which makes them attractive for solar energy applications. COHP study illustrates that strong Bi-chalcogen bonding characterizes the valence band, whereas antibonding states prevail above the Fermi level in both Bi_2PbSe_4 and Bi_2PbTe_4 . Their promise as absorber materials in photovoltaic devices is highlighted by optical investigations that show considerable absorption in the visible and infrared ranges, high dielectric constants, and higher photoconversion performance. The Seebeck coefficient, lattice thermal conductivity, and electrical conductivity were employed to assess thermoelectric features. These ternary materials are suitable for integrated solar energy collecting and conversion systems because of their outstanding optical absorption and thermoelectric potential. The structure–property interactions of these materials are explained by this study, opening the door for testing and more optimization for improved energy devices.

Received 10th May 2025
Accepted 22nd August 2025

DOI: 10.1039/d5ra03284a

rsc.li/rsc-advances

1. Introduction

Due to the rapid rise in carbon production and global warming caused by fossil fuel consumption, there has been a significant global focus across multiple industries on providing clean energy and reducing greenhouse gases.^{1–4} Globally, solar (PV) technology is growing at the fastest rate among energy technologies. It is now more inexpensive than fossil fuels, with costs that are almost 90% lower.⁵ The worldwide energy supply from solar cells is 2%, but this might increase greatly if manufacturing challenges are successfully handled.⁶ The semiconductor compounds used in producing photovoltaic solar sheets have an important effect on solar cell production.^{7–9}

To overcome the barriers and limitations that prevent the widespread use of solar panels, extensive experimental and theoretical research has been recently conducted to identify compounds that are both highly effective and reasonably priced for use in solar panel design and manufacture.^{10–13} The ability of semiconductor materials to absorb solar energy is heavily influenced by their energy conversion efficiency, which is directly proportional to their energy band gap. Because of their optoelectronic capabilities, semiconductor materials are vital for the progress of optoelectronic devices and manufacturing methods.^{14–17} Unlike optically active direct band gap semiconductors, which perform well, optically inert indirect band gap semiconductors are inefficient because optical transitions need the involvement of phonons.^{18,19} With the increasing necessity for environmentally approachable and renewable energy resources in recent times, thermoelectric compounds have received a lot of attention.^{20–24} The figure of merit governs a thermoelectric material's energy conversion efficiency. Recently, the TE behavior of IV–V–VI materials has sparked attention in the thermoelectrical field due to their small thermal conductivity. Y. Gan *et al.* anticipate 56 exceptional semiconductors from the family IV–V–VI (IV = Ge, Sn, Si, Pb; V

^aDepartment of Physics, College of Science, Imam Mohammad Ibn Saud Islamic University (IMSIU), Riyadh, 13318, Saudi Arabia

^bNational University of Sciences and Technology (NUST), Islamabad, Pakistan

^cDepartment of Physics, Abdul Wali Khan University, Mardan, 23200, Pakistan. E-mail: salmankhan73030@gmail.com

^dUniSA Science and Medicine Foundation Centre, Universiti Sultan Zainal Abidin, Gong Badak Campus, 21300 Kuala Nerus, Terengganu, Malaysia

^eLaboratory of Physical Engineering, Department of Physics, Faculty of Matter Sciences, University of Tiaret, Algeria



= Sb, Bi, As; VI = S, Se, Te) and show that the majority of these materials have thermal conductivity less than $1.0 \text{ W m}^{-1} \text{ K}^{-1}$ at normal temperature.²⁵ PbBi_2S_4 material exhibits very small lattice thermal conductivity of $0.46 \text{ W m}^{-1} \text{ K}^{-1}$ around the temperature range at 800 K, with a value of zT of 0.46.²⁶ Singh *et al.*²⁷ discovered Bi_2GeTe_4 to be an n-type material having a zT value of 0.10 and a small value of $S^2\sigma$ of about $1.54 \mu\text{W cm}^{-1} \text{ K}^{-2}$ at temperature of 350 K. Bi_2GeTe_4 IV–V–VI ternary thermoelectric material was studied to have near-room temperatures of small thermal conductivity of $0.28 \text{ W m}^{-1} \text{ K}^{-1}$ at 350 K.²⁷ Schroeder *et al.*²⁸ first stated that p-type Bi_2GeTe_4 has a zT of 0.050 at ambient temperature. Konstantinov *et al.*²⁹ exposed that Bi_2GeTe_4 exhibits relatively adjacent p–n transition point with slight Ge content adjustments, implying that the E_F of Bi_2GeTe_4 would be in the middle of the energy gap. The electrical band structures of bulk Bi_2GeTe_4 , both with and without SOC, exhibit a limited band gap. Spin orbit coupling is vital in forecasting proper dispersion when the energy band gap increases from 0.380 eV (LDA) to $\sim 0.1 \text{ eV}$ (LDA + SOC), which is near the described bulk band gap of $\sim 0.18 \text{ eV}$.^{30–34} Due to their potential uses in optoelectronics and thermoelectric devices, the electrical, optical, and thermoelectric properties of Bi_2PbSe_4 and Bi_2PbTe_4 have been extensively studied here using Density Functional Theory (DFT). The potential of Bi_2PbSe_4 and Bi_2PbTe_4 as cutting-edge materials for energy conversion technologies is emphasized by these results. Though additional experimental validation and investigation of doping methods are required to fully demonstrate their potential for practical use, yet DFT has proven to be a useful tool for comprehending and optimizing their properties.

2. Computational method

The structural parameters of Bi_2PbCh_4 (Ch = Se and Te) materials as well as their electronic properties, were computed using the (FP-LAPW) approach employed in the WIEN2k code.³⁵ The PBE-GGA was used to analyze the effects of electronic interchange and correlation on structural characteristics. It is well accepted that energy gaps anticipated using typical approximations are smaller than observed.³⁶ Tran and Blaha formed a novel, useful potential known as the Tran–Blaha modified Beck–Johnson (TB-mBJ) potential, which gives a more accurate depiction of electrical characteristics and band gap predictions.³⁷ The cut-off value for the plane wave basis set K_{max} was established as $R_{\text{min}} \times \text{MT} = 11$ (where $R_{\text{min}} \times \text{MT}$ is the minimal radii of the muffin-tin sphere). We replaced the Brillouin zone integration with a total k -points of $14 \times 14 \times 8$ Monkhorst–Pack. The self-consistent field repetitions continued till the crystal's whole energy was less than 10^{-5} Ry . The Crystal Orbital Hamilton Population (COHP) calculations were carried out using the electronic structures acquired from Quantum ESPRESSO,³⁸ which were then post-processed to give the projected COHP curves for vital atomic pairs. Together with the Boltzmann transport calculations, including the rigid group and continually decreasing time approximations utilized in the BoltzTraP package, the thermodynamic properties were calculated using first-principles methods.³⁹

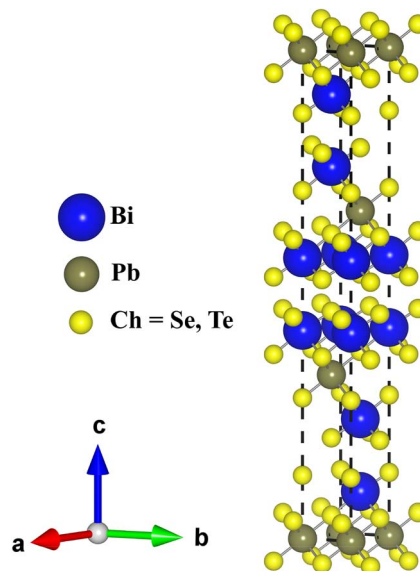


Fig. 1 The crystal structure for the Bi_2PbCh_4 (Ch = Se, Te) chalcogenides.

3. Results and discussions

3.1 Structure properties

Bi_2PbSe_4 has a trigonal crystal structure with $R\bar{3}m$ space group (see Fig. 1). Pb^{2+} is connected to six identical Se^{2-} atoms, forming PbSe_6 octahedra, which have edges with six identical BiSe_6 octahedra, corners with six corresponding PbSe_6 octahedra, and corners with six identical BiSe_6 octahedra. The length of every Pb–Se bond measures 3.06 \AA . Bi^{3+} is linked with six Se^{2-} , forming octahedra BiSe_6 , which attach corners and edges to three identical PbSe_6 octahedra and edges with six extra BiSe_6 octahedra. Three of the Bi–Se bond lengths measure 2.75 \AA , while three others measure 3.06 \AA . Two non-equivalent Se^{2-} sites exist. In the first Se^{2-} site, three corresponding Bi^{3+} atoms form bonds with Se^{2-} in a three-coordinate arrangement. The second site, for Se^{2-} is connected to three equivalent Pb^{2+} atoms and three equivalent Bi^{3+} atoms, resulting in a grouping of edge- and corner-sharing SeBi_3Pb_3 octahedra. Bi_2PbSe_4 have a trigonal crystal structure with $R\bar{3}m$ space group. Six corresponding Te^{2-} atoms bond with Pb^{2+} to produce PbTe_6 octahedra, sharing corners with six similar BiTe_6 octahedra and corners with six corresponding PbTe_6 and BiTe_6 octahedra. The length of each Pb–Te bond measures 3.17 \AA . Six Te^{2-} atoms bond with Bi^{3+} to produce BiTe_6 octahedra, which combine corners and edges with three equivalent PbTe_6 octahedra and six equivalent BiTe_6 octahedra. Two inequivalent Te^{2-} sites exist. In the first Te^{2-} site, three Bi^{3+} atoms form bonds with Te^{2-} atoms. Also Te^{2-} atoms connects to three Pb^{2+} atoms and three identical Bi^{3+} atoms, resulting in an association of corner- and edge-sharing $\text{Bi}_3\text{Pb}_3\text{Te}$ octahedra. The energy and volume optimization plots for Bi_2PbSe_4 and Bi_2PbTe_4 show the link between the system's total energy and unit cell volume. Table 1 presents the atomic coordinates and lattice constants of two chalcogenides: Bi_2PbSe_4 and Bi_2PbTe_4 . Likewise Bi_2PbSe_4



Table 1 The coordinates of atomic sites, lattice constants bulk modulus, ground state energy, and equilibrium volume for Bi_2PbCh_4 (Ch = Se, Te) chalcogenides

Materials	PBE-GGA				a (Å)	b (Å)	c (Å)	B_0 (GPa)	E_0 (Ry)	V_0 (Å ³)
$\text{Bi}_2\text{PbSe}_4(R\bar{3}m)$	Atoms	x	y	z	4.78	4.78	32.27	74.78	−148.32	289.09
	Bi	0.376	0.697	0.263						
	Pb	0.387	0.635	0.698						
	Se	0.686	0.359	0.058						
$\text{Bi}_2\text{PbTe}_4(R\bar{3}m)$	Atoms	x	y	z	4.95	4.95	32.89	62.35	−174.65	323.16
	Bi	0.381	0.737	0.371						
	Pb	0.394	0.672	0.719						
	Te	0.745	0.473	0.069						

possesses lattice constants of $a = b = 4.78$ Å and $c = 32.27$ Å, while Bi_2PbTe_4 has slightly greater values of $a = b = 4.95$ Å and $c = 32.89$ Å. The increased lattice parameters for Bi_2PbTe_4 can be related to the greater atomic radius of tellurium (Te) compared to selenium (Se). This results in a general expansion of the crystal lattice when Te replaces Se. Bi_2PbSe_4 possesses larger cell dimensions, implying a more relaxed structure because of weaker bonding and increased polarizability of Te atoms. The atomic locations indicate that the Bi, Pb, and chalcogen atoms possess separate fractional coordinates along the x , y , and z dimensions. In Bi_2PbSe_4 , Bi is at (0.376, 0.697, 0.263), Pb at (0.387, 0.635, 0.698), and Se at (0.686, 0.359, 0.058). In Bi_2PbTe_4 the Bi, Pb, and Te atoms have positions at (0.381, 0.737, 0.371), (0.394, 0.672, 0.719), and (0.745, 0.473, 0.069), respectively. The shift in atomic coordinates for Bi and Pb between the two materials indicates that chalcogen substitution caused small shifts in bonding environments and interatomic distances. In particular, the chalcogen atoms (Se and Te) have different spatial arrangements, especially in the x and y dimensions, which could influence electronic distribution and local symmetry. In general, these structural differences, though modest, are vital for understanding the materials' electronic, optical, and thermoelectric properties, as these come directly from the interaction of atomic size and lattice geometry. Fig. 2(a) and (b) can be fitted with models based on the Birch–Murnaghan equation of state to get parameters such as bulk modulus, equilibrium volume, and pressure derivatives. The lowest point on the curve, 1460 Å³ for Bi_2PbSe_4 and 1725.4 Å³ for Bi_2PbTe_4 , represents the balance volume (V_0), where the compound is more stable. At this volume, the system's energy is minimized, indicating the most energetically favorable structure. The two graphs show the optimization of energy vs. volume for the materials Bi_2PbSe_4 and Bi_2PbTe_4 . The equilibrium volume is often calculated using (DFT) computations, and these curves show the system's whole energy as a function of its unit cell volume. The parabolic form of both graphs displays that the energy spreads its least value at a specific volume, which is the material's equilibrium configuration. The curvature of the E – V curve for Bi_2PbSe_4 near equilibrium volume is steeper compared to Bi_2PbTe_4 , implying a relatively higher bulk modulus. The wider curve for Bi_2PbTe_4 , on the other hand, represents greater compressibility and less stiffness. The equilibrium volume difference between the two materials is

highlighted by the minima's position along the volume axis, which reproduces their different structural characteristics. The greater equilibrium volume (V_0) for Bi_2PbTe_4 (see Table 1) illustrates Te's larger ionic radius compared to Se. Bi_2PbSe_4 possesses greater bulk modulus, implying more incompressibility than Bi_2PbTe_4 .

3.2 Electronic properties

The Crystal Orbital Hamilton Population (COHP) plots (see Fig. 3(a) and (b)) demonstrate bonding and antibonding interactions between key atomic pairs such as Bi–Pb, Bi–Se (Bi–Te), and Pb–Se (Pb–Te), as well as the total COHP across the valence and the conduction band. In both materials, negative COHP values suggest bonding interactions, whereas positive values imply antibonding states. Strong bonding dominates Bi_2PbSe_4 in the energy range from roughly -6 eV to just below E_F , with the most intense bonding peaks resulting from Bi–Se and Pb–Se interactions, especially at -5 eV and -2 eV, consistent with the strong covalent character between Bi/Se and Pb/Se. The Bi–Pb interaction additionally shows bonding behavior in this location, though to a lesser extent, reflecting weak covalency. Additionally, as the energy approaches E_F from below, the COHP curves for Bi–Se and Pb–Se fall quickly to zero before crossing into minor positive values, showing the onset of antibonding states. Above E_F , particularly in the conduction band region (0 to $+3$ eV), the total COHP is mostly positive, dominated by antibonding states from Bi–Se and Pb–Se, indicating that more electrons might destabilize the structure by populating antibonding orbitals. The heavier and more polarizable Te atom produces a little shift in bonding in Bi_2PbTe_4 . Bi–Te interactions display strong bonding features deeper in the valence band (-5.5 to -2 eV), but with larger peaks than Bi–Se, signifying more delocalized bonding. Pb–Te contributions are significantly lower over the energy range, illustrating that Pb and Te have low covalency in comparison to Pb–Se. Bi–Pb interactions in Bi_2PbTe_4 are stronger than in Bi_2PbSe_4 , particularly at -4 eV and -1 eV. This indicates that Te substitution promotes Bi–Pb overlap, potentially because of structural modifications that decrease Bi–Pb distances or change orbital orientation. As we approach E_F , Bi–Te bonding weakens and transitions into antibonding states close to the Fermi level, with a sharp positive peak between $+0.5$ and $+2$ eV, indicating that



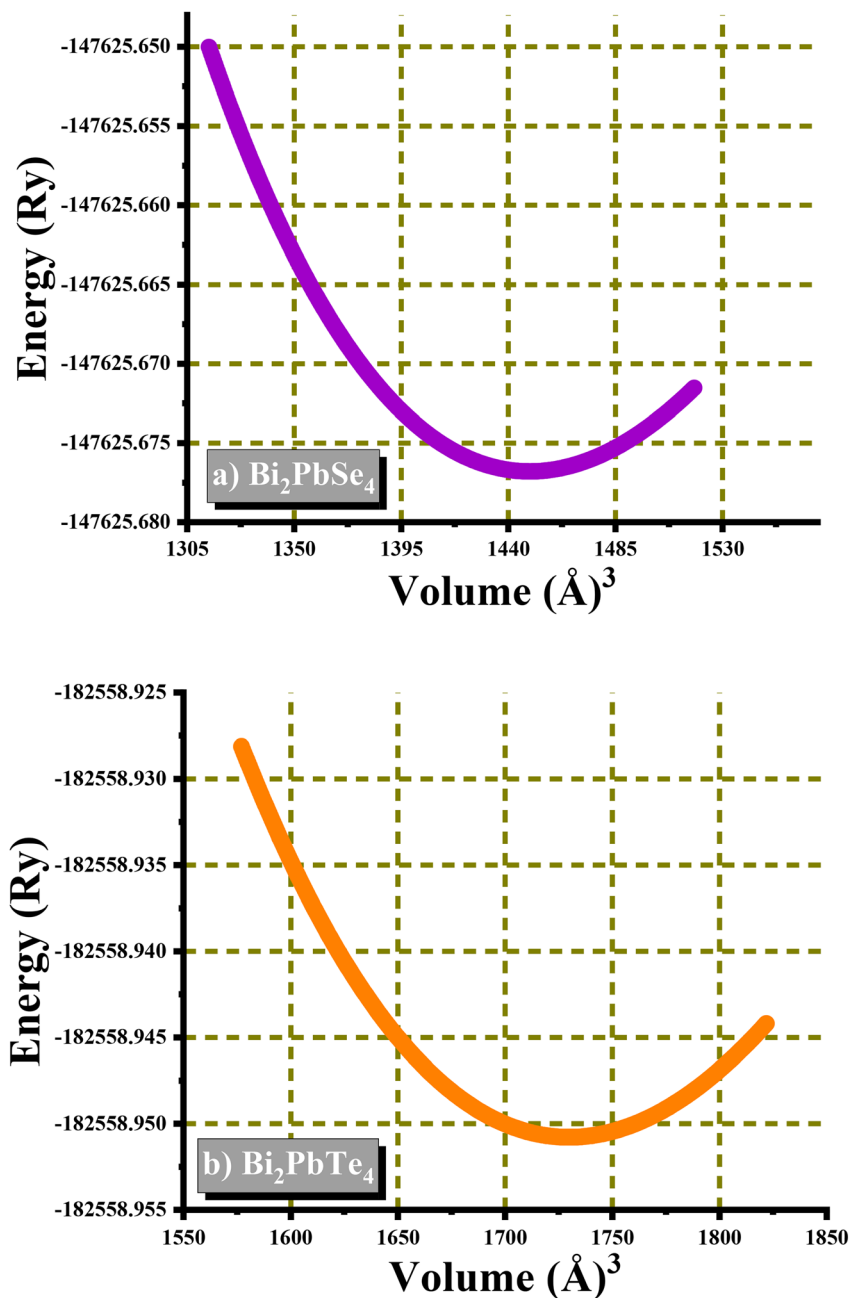


Fig. 2 The optimization plots for the (a) Bi_2PbSe_4 and (b) Bi_2PbTe_4 chalcogenides.

electron doping could swiftly destabilize Bi–Te bonds. The total COHP for Bi_2PbTe_4 shows an important antibonding region directly above E_F , however, with slightly smaller intensity than Bi_2PbSe_4 . This implies that Bi_2PbTe_4 may tolerate modest electron doping compared to Bi_2PbSe_4 before structural destabilization occurs. Bi_2PbTe_4 exhibits higher Pb–anion bonding (Pb–Se) and a somewhat more symmetric bonding/antibonding distribution, whereas Bi_2PbTe_4 focuses on Bi–Pb and Bi–Te pairs, with Pb–Te bonds having little impact on overall stability. This is in line with the decreased electronegativity difference between Pb and Te, which reduces bond polarity and overlap strength. The deeper and sharper bonding peaks in Bi_2PbSe_4 show a more localized covalent framework, while the broader

peaks in Bi_2PbTe_4 imply higher orbital delocalization as well as a more metallic nature. The COHP study reveals that both compounds exhibit strong Bi–chalcogen bonds in the valence band, but differ in their secondary bonding routes. Pb–Se plays a role in Bi_2PbSe_4 , while Bi–Pb becomes more relevant in Bi_2PbTe_4 . Electron doping can affect bonding integrity, as antibonding states dominate the conduction bands in both cases. However, Bi_2PbTe_4 has a smaller total antibonding peak at E_F , suggesting slightly more tolerance to these effects. Bi_2PbSe_4 's stronger covalency could favor lower carrier mobility but higher lattice stability, while Bi_2PbTe_4 's more delocalized bonding may enhance carrier transport at the expense of less effective anion-cation binding.

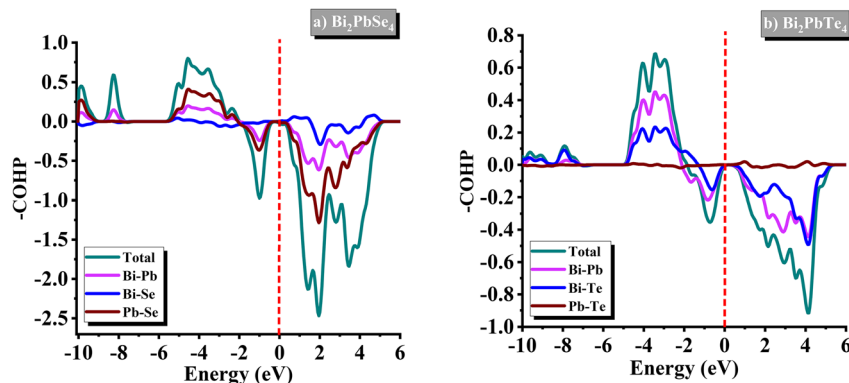


Fig. 3 The Crystal Orbital Hamilton Population (COHP) plots for (a) Bi_2PbSe_4 and (b) Bi_2PbTe_4 chalcogenides presenting the total and pairwise orbital interactions between Bi–Pb, Bi–Se/Te, and Pb–Se/Te. Negative COHP values correspond to the bonding states, whereas the positive values correspond to antibonding states.

To recognize the distribution of electronic states, the density of states in energy ranging from -8.0 to 8.0 eV was determined. By calculating the partial density of states for Bi_2PbSe_4 and Bi_2PbTe_4 , we studied the electron distribution in the valence band (VB) and conduction band (CB). Fig. 4(a) and (b) depicts

the partial density of states of both Bi_2PbSe_4 and Bi_2PbTe_4 in the VB and CB regions. Bi-p orbitals strongly hybridize with p states of Se and Te, ranging from -4.8 eV to 0 eV. The bonding performance of Bi and Se/Te is largely covalent, with the Bi-p orbitals contributing to the expansion of bonding states. The Bi-d and Bi-s orbitals are less complicated in bonding because they are more confined. As a result, their contributions to the VB are low and limited to a higher energy range -2.0 eV to 0 eV. Because they are involved in making antibonding states with Se/Te-p orbitals, Bi-p states make a main impact in the CB from 1.0 eV– 6.0 eV. These antibonding states arise at higher energy levels as a result of atomic orbital repulsion. At higher energy levels, 6.0 eV to 6.5 eV, the contribution of Bi-d states is small because of the maximum energy and less important function in generating the conduction band. For Bi_2PbSe_4 and Bi_2PbTe_4 , the experimental contributions of s and p states of Pb in the VB and CB, as well as the substantial existence of Pb-s states from -7.8 eV to -6.3 eV, show that these orbitals are deeply bonded and belong to the lower-energy valence band. This is characteristic of s-orbitals, which are more limited and have lower energy due to their round symmetry and close overlap with the nearby atomic potentials. The Pb-s states also contribute, albeit less significantly, between -1.0 eV and the Fermi level. This shows hybridization with other orbitals, such as the Bi-p and Se/Te-p states, which results in bonding and antibonding states nearer 0 eV. Pb-p states lead the conduction band between 1.8 and 7.0 eV. This is because Pb-p states have with larger energy than Pb-s states and can efficiently overlap with the antibonding states formed by hybridization with the surrounding Bi-p and Se/Te-p states. The observed dominance of p states of Se and Te in the valence band in the energy range -4.5 eV to the Fermi level and CB from 1.5 eV to 6 eV for Bi_2PbSe_4 and Bi_2PbTe_4 compounds. This happens because p states of Se and Te are energetically well-positioned to establish strong covalent bonding and antibonding states with the lattice adjacent atoms, especially Bi and Pb. The CB is formed by antibonding combinations of the p states of chalcogens, along with some additional influence from other orbitals (e.g., s/d-states) of Se, Te, and nearby Bi and Pb atoms.

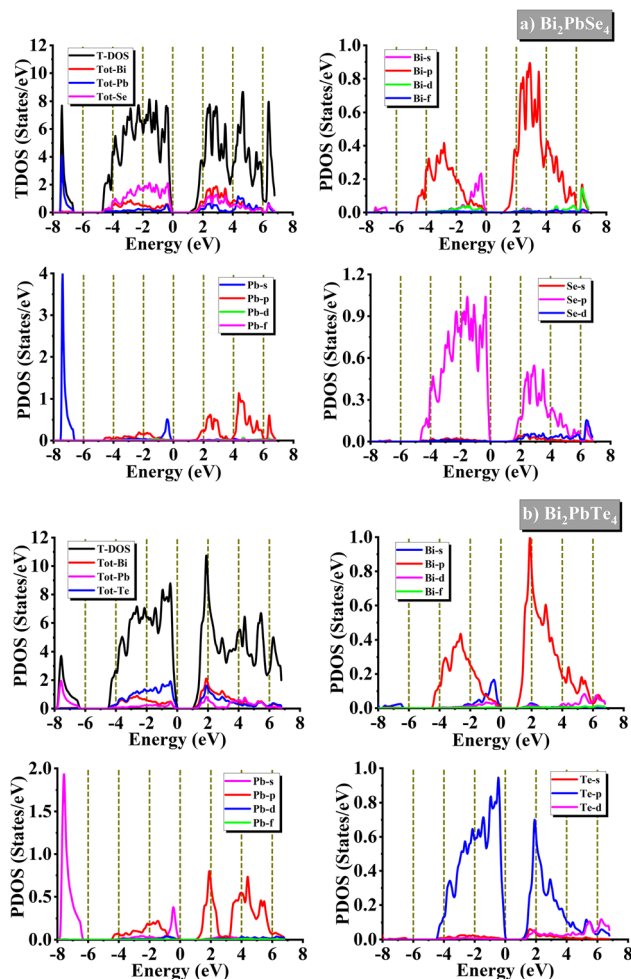


Fig. 4 The projected density of states for (a) Bi_2PbSe_4 and (b) Bi_2PbTe_4 chalcogenides.



contribute less to bonding because they are more localized and lower in energy than the p-orbitals. Their contributions to that conduction band in that energy range of 1.8 eV to 6.3 eV are attributable to hybridization at higher energy levels.

Fig. 5(a)–(d) depicts the projected EB structures for these Bi_2PbSe_4 and Bi_2PbTe_4 compounds at their balanced structural parameters, comparing the PBE-GGA and TB-mBJ methods. Bi_2PbSe_4 and Bi_2PbTe_4 have similar energy band characteristics. The energy gap of both Bi_2PbSe_4 and Bi_2PbTe_4 is noticed as direct (Γ – Γ). The energy gaps with the TB-mBJ and PBE-GGA are 1.12 and 0.71 eV for Bi_2PbSe_4 and 1.08 and 0.82 eV for Bi_2PbTe_4 . Where Bi_2PbSe_4 has a slightly larger band gap than Bi_2PbTe_4 under both the TB-mBJ and PBE-GGA methods, since selenium (Se) is smaller and less electronegative than tellurium. Stronger

bonding in Bi_2PbSe_4 causes a wider energy difference, resulting in larger band gap. Bi_2PbTe_4 has weaker bonding due to the greater size and higher polarizability of Te, resulting in a smaller band gap. The electronic band structure and orbital contributions reported for Bi_2PbSe_4 and Bi_2PbTe_4 are determined by their atomic composition, chemical bonding type, and orbital hybridization. Because of their large atomic number, bismuth (Bi) atoms provide a significant contribution to the valence band, resulting in relativistic effects. These effects induce a considerable splitting of energy levels, resulting in the stabilization of Bi-p states from -4.8 eV to the Fermi level maximum. Lead (Pb) atoms contribute *via* their s-orbitals at -7.8 to -6.3 eV. This is due to the lower energy of Pb-s states, which are predominantly involved in core-like bonding

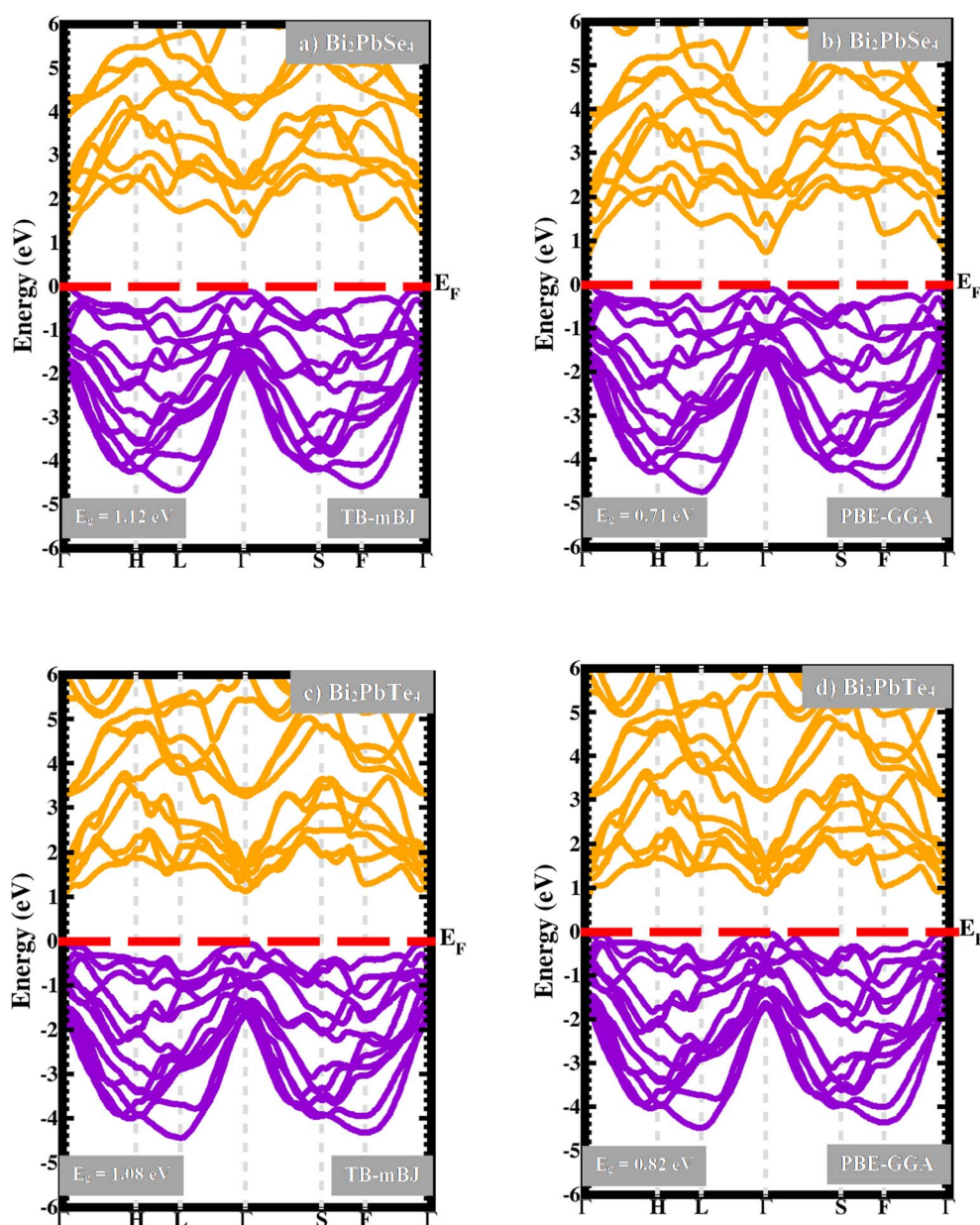


Fig. 5 The energy band profiles for (a and b) Bi_2PbSe_4 and (c and d) Bi_2PbTe_4 chalcogenides.

interactions. Their contribution to bonding is less important than that of Bi-p or chalcogen-p states; hence, they are further down the valence band. The overlap of Bi-p and Se/Te-p states gives bonding and antibonding states in the VB. Bi-p states lead in the CB between 1.0 and 6.0 eV due to the antibonding character of the Bi-p and chalcogen-p connections. Pb-p states are more energetic than Pb-s states and contribute importantly to the CB between 1.8 and 7.0 eV. This is because Pb-p states overlap weakly with Bi-p states and donate antibonding interactions, causing them to scatter across the CB. In the 1.5 to 6.01 eV range, these Se-p and Te-p states contribute through hybridization with the p states of Bi and Pb. The chalcogen-p states mainly control the (DOS) around the CBM.

3.3 Optical properties

The real part of the frequency-dependent dielectric constant $\varepsilon_1(\omega)$ delivers key information regarding the optical nature of materials such as Bi_2PbSe_4 and Bi_2PbTe_4 . Fig. 6(a) illustrates the $\varepsilon_1(\omega)$ in Bi_2PbSe_4 and Bi_2PbTe_4 . Bi_2PbSe_4 and Bi_2PbTe_4 have $\varepsilon_1(0) = 15.0$ and 20.0 , respectively. A higher value for the Bi_2PbTe_4 suggests more polarizability and lower interband transition energy than Bi_2PbSe_4 . Moreover, Bi_2PbTe_4 has a lower band gap at 2.0 eV compared to Bi_2PbSe_4 at 2.5 eV. The peaks in $\varepsilon_1(\omega)$ indicate resonances caused by electrical transitions between bands. The lower peak energy of Bi_2PbTe_4 indicates that its band structure has smaller energy gaps for some optical transitions than Bi_2PbSe_4 . Following the peaks, $\varepsilon_1(\omega)$ drops, and Bi_2PbSe_4 and Bi_2PbTe_4 reach negative $\varepsilon_1(\omega)$ values at 3.0 and 2.5 eV, respectively. When $\varepsilon_1(\omega)$ goes negative, the material exhibits metallic optical behavior (plasmonic behavior). This phenomenon results from a strong interaction between free

charge carriers and incident light; Bi_2PbTe_4 achieves this state quickly because of its larger carrier density and more delocalized electrons. The imaginary part of the dielectric function, $\varepsilon_2(\omega)$, represents absorption of electromagnetic radiation caused by interband electronic transitions. Fig. 6(b) indicates that the threshold values of the $\varepsilon_2(\omega)$ are 1.5 eV and 1.0 eV for Bi_2PbSe_4 and Bi_2PbTe_4 , respectively. The threshold value is the negligible energy required for interband electronic transitions. The highest peaks were seen at 3.0 and 2.5 eV for Bi_2PbSe_4 and Bi_2PbTe_4 , respectively. Bi_2PbTe_4 drop to lower energy indicates a denser and more accessible conduction band structure than in Bi_2PbSe_4 . After the peak, the imaginary part declines because fewer electron states exist for high-energy transitions. This drop is normal as photon energy rises over the threshold where interband transitions dominate, leaving only weaker transitions or higher-order effects.

Fig. 6(c) depicts how the refractive index $n(\omega)$ varies with photon energy for materials Bi_2PbSe_4 and Bi_2PbTe_4 . The static $n(0)$ values for Bi_2PbSe_4 and Bi_2PbTe_4 are 3.8 and 4.6, respectively. The $n(\omega)$ first rises due to the intense resonance from interband electronic transitions. The highest peaks are 2.8 eV for Bi_2PbSe_4 and 2.3 eV for Bi_2PbTe_4 . The transitions resonate with the input photon energy, resulting in higher polarizability and a high refractive index. Bi_2PbSe_4 has a greater band gap than Bi_2PbTe_4 , resulting in a peak at somewhat higher photon energy. The heavier Te atom enhances spin-orbit coupling and polarizability in Bi_2PbTe_4 , resulting in a higher static refractive index. At higher energies, materials show plasma oscillations of free carriers or interband transitions, which minimize the contribution of bound electrons to the refractive index. The $n(\omega)$ declines for both materials when photon energy increases from 2.8 eV to 24.0 eV in Bi_2PbSe_4 and from 2.3 eV to 24.0 eV in

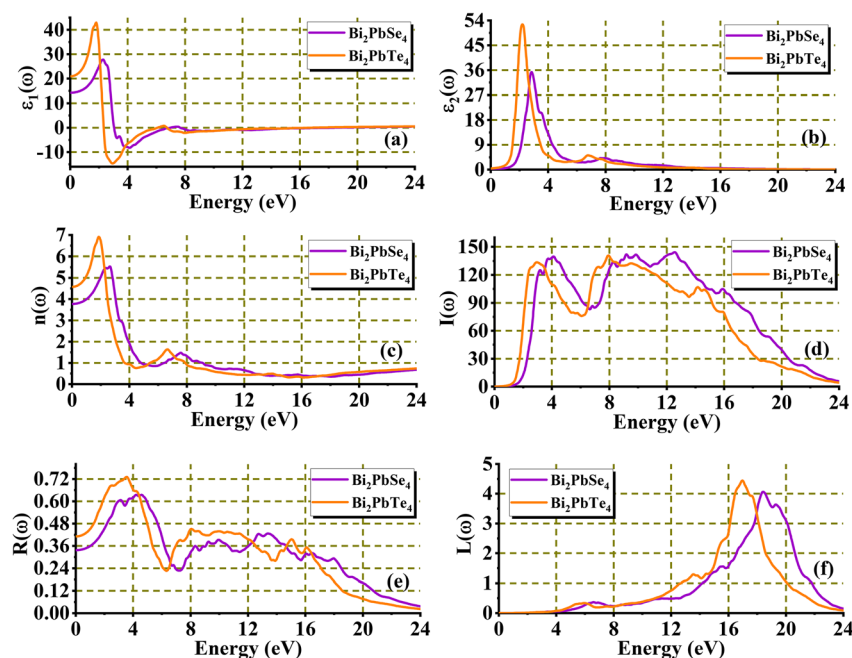


Fig. 6 Calculated optical properties of Bi_2PbCh_4 (Ch = Se, Te): (a) and (b) dielectric function components, (c) refractive index, (d) absorption coefficient, (e) reflectivity spectra, and (f) energy loss function.



Bi_2PbTe_4 . Fig. 6(d) shows the observed trend in the absorption coefficient $I(\omega)$ for Bi_2PbSe_4 and Bi_2PbTe_4 materials. The threshold absorption coefficient represents the minimal photon energy essential to stimulate an electron from the VB to the CB. Bi_2PbSe_4 at 1.6 eV and Bi_2PbTe_4 at 1.3 eV have values near their band gap energies. This is when interband transitions begin, resulting in considerable absorption. In the photon energy range of 3.5 eV to 12.5 eV for Bi_2PbSe_4 and 2.7 eV to 12.0 eV for Bi_2PbTe_4 , substantial absorption occurs due to transitions between deeper valence bands and higher conduction bands. These transitions entail a denser electronic state distribution, resulting in a larger density of optical transitions and, thus, higher absorption coefficients. Due to Bi_2PbTe_4 lower band gap, the range begins significantly earlier at 2.7 eV than Bi_2PbSe_4 at 3.5 eV. The specific electronic structure of Bi_2PbSe_4 and Bi_2PbTe_4 dictates where major transitions terminate. Beyond 12.5 eV (Bi_2PbSe_4) and 12.0 eV (Bi_2PbTe_4), the states no longer line well with the incoming photon energy, resulting in decreased absorption.

Fig. 6(e) shows that Bi_2PbSe_4 and Bi_2PbTe_4 have $R(0)$ of 0.35 and 0.40, respectively, indicating the material's inherent capacity to reflect light in the low-energy regime. Differences in $R(0)$ result from changes in the electronic structure, particularly the DOS at or around the Fermi energy. Bi_2PbSe_4 and Bi_2PbTe_4 have the largest $R(\omega)$ peaks at 4.3 eV and 3.8 eV, respectively. The discrepancy in peak positions (4.3 eV vs. 3.8 eV) indicates differences in the band structure of Bi_2PbSe_4 and Bi_2PbTe_4 . Bi_2PbTe_4 has a smaller energy gap between the electronic states involved in this optical transition. The band structures of Bi_2PbSe_4 and Bi_2PbTe_4 differ due to the replacement of selenium with tellurium. Tellurium, being heavier, causes higher spin-orbit coupling and potentially narrower band gaps. At higher photon energies, the materials absorb light due to the start of various transitions or the excitation of electrons to states deep in the conduction band, diminishing total reflectivity. The $L(\omega)$, including its peaks and subsequent reduction, is intimately related to optical characteristics and collective excitations in the material. In Fig. 6(f), the threshold energy of $L(\omega)$ is 4.2 eV for Bi_2PbSe_4 and 4.0 eV for Bi_2PbTe_4 , indicating the start of considerable energy loss. This threshold frequently coincides with interband transitions or excitations, in which an electron jumps between energy bands and bridges the band gap. The largest peaks at 18.50 eV for Bi_2PbSe_4 and 16.7 eV for Bi_2PbTe_4 parallel to the plasmon resonance frequency, which occurs when the conduction electrons' collective oscillations match the incident electromagnetic wave. The energy loss function $L(\omega)$ for Bi_2PbSe_4 and Bi_2PbTe_4 declines after reaching 18.5 eV and 16.7 eV, respectively. The dielectric function $\epsilon(\omega)$ is less sensitive at higher frequencies due to electrons' inability to follow the quickly fluctuating field, resulting in a decreased $L(\omega)$.

3.4 Thermoelectric properties

The behavior of the Seebeck coefficient (S) can be explained using the fundamental physics of thermoelectric materials, specifically the link between carrier concentration, scattering mechanisms, and temperature. Fig. 7(a) depicts the S for

Bi_2PbSe_4 and Bi_2PbTe_4 materials at temperatures ranging from 0 to 700 K. Fig. 7(a) shows that Bi_2PbSe_4 and Bi_2PbTe_4 have maximal Seebeck coefficient values of $1.5 \times 10^{-6} \text{ V K}^{-1}$ and $3.01 \times 10^{-6} \text{ V K}^{-1}$ at 50 K, respectively. Bi_2PbTe_4 has a larger initial Seebeck coefficient at 50 K than Bi_2PbSe_4 due to variations in their band structures, carrier effective masses, and intrinsic doping levels. At low temperatures, the carrier density is low, resulting in a sharper energy dependency of the density of states and superior thermopower. The carriers are less thermally restless, and the transport properties are mostly dictated by the compound's basic electronic structure. This allows for larger asymmetry in the carrier energy distribution, resulting in a higher Seebeck coefficient (S). Higher temperatures cause thermal excitation of electrons and holes around the band gap, enhancing bipolar conduction. The Seebeck coefficient, which is the weighted number of contributions from both types of carriers, reduces as they tend to counterbalance one another. At 650 K, Bi_2PbSe_4 and Bi_2PbTe_4 have minimal Seebeck coefficients (S) of $-12.5 \times 10^{-6} \text{ V K}^{-1}$ and $-13.0 \times 10^{-6} \text{ V K}^{-1}$, respectively. The negative value shows that electrons are the main charge carriers in each Bi_2PbSe_4 and Bi_2PbTe_4 . Bi_2PbTe_4 has a much larger negative Seebeck coefficient (S) at 650 K, representing stronger n-type behavior, which could be owing to a lesser band gap or more thermal carrier excitation. The reduction in electrical conductivity (σ/τ) for both Bi_2PbSe_4 and Bi_2PbTe_4 can be clarified by the interaction of carrier concentration, mobility, and scattering mechanisms. At higher temperatures, thermal excitation causes a slight rise in intrinsic carriers. However, this is inadequate to compensate for the considerable drop in mobility caused by scattering effects. Fig. 7(b) displays a reduction in electrical conductivity (σ/τ) from 50 K to 650 K for both Bi_2PbSe_4 and Bi_2PbTe_4 . Fig. 7(b) shows that the maximum electrical conduction (σ/τ) numbers at 50 K are 1.44×10^{18} and $1.42 \times 10^{18} \text{ } \Omega \text{ ms}^{-1}$ for Bi_2PbSe_4 and Bi_2PbTe_4 , respectively. At 650 K, Bi_2PbSe_4 and Bi_2PbTe_4 have minimum electrical conductivity (σ/τ) values of 1.36×10^{18} and $1.32 \times 10^{18} \text{ } \Omega \text{ ms}^{-1}$, respectively.

Bi_2PbSe_4 and Bi_2PbTe_4 display a linear increase in electronic thermal conductivity (κ_e) with temperatures from 50 K to 650 K, which could be credited to that material's electronic characteristics. Fig. 7(c) indicates a linear rise in electronic heat conductivity (κ_e) through temperature from 50 K to 650 K for Bi_2PbSe_4 and Bi_2PbTe_4 . The Wiedemann–Franz law describes that electronic thermal conductivity (κ_e) is determined by the mobility of charge carriers in a material and is proportional to its electrical conductivity (σ): $\kappa_e = L\sigma T$. Since T is directly in the Wiedemann–Franz equation, κ_e increases with temperature as long as σ does not fall significantly. Bi_2PbSe_4 and Bi_2PbTe_4 materials have a thermal conductivity of 0.90 and 1.05 ($\times 10^{14} \text{ W m}^{-1} \text{ K}^{-1} \text{ s}^{-1}$) at -300 K , respectively, and reach an extreme of 1.95 and 2.10 ($\times 10^{14} \text{ W m}^{-1} \text{ K}^{-1} \text{ s}^{-1}$) at partial density of states 600 K. Bi_2PbTe_4 has a lower band gap than Bi_2PbSe_4 , resulting in higher carrier concentration at a given temperature and, thus, higher κ_e . The figure of merit zT for both materials (see Fig. 7(d)) surges as temperature rises from 50 K to 650 K. Fig. 7(d) indicates that at 300 K, Bi_2PbSe_4 and Bi_2PbTe_4 had zT values of 0.25 and 0.20, respectively. At 650 K, the highest zT



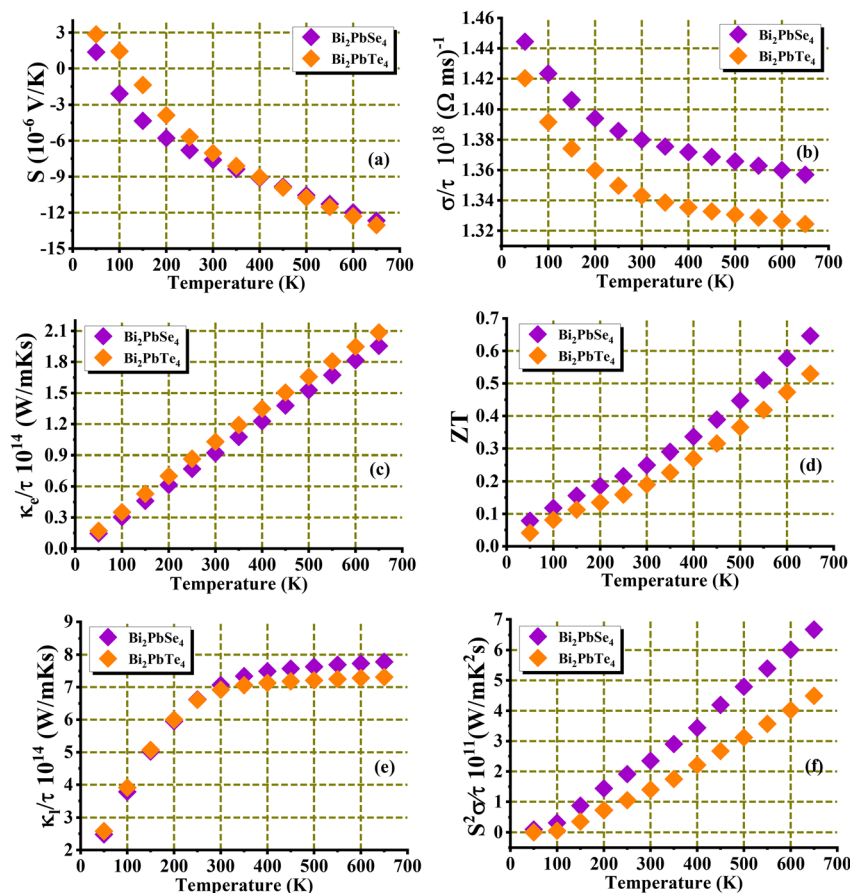


Fig. 7 Calculated thermoelectric properties of Bi_2PbCh_4 ($\text{Ch} = \text{Se}, \text{Te}$): (a) Seebeck coefficient, (b) electrical conductivity, (c) thermal conductivity, (d) figure of merit, (e) lattice thermal conductivity, and (f) power factor.

values are 0.65 and 0.53, respectively. Differences and trends in zT values occur as thermoelectric characteristics fluctuate with temperature. At low temperatures (300 K), both materials have a low zT due to limited carrier excitation and increased thermal conductivity. Bi_2PbSe_4 and Bi_2PbTe_4 differ in their fundamental material features, including bonding strength, atomic masses, and phonon scattering mechanisms. Bi_2PbSe_4 often performs better in thermoelectric applications because of reduced thermal conductivity and a more favorable combination of electrical characteristics.

The lattice thermal conductivity (κ_l) and power factor (PF) of Bi_2PbSe_4 and Bi_2PbTe_4 show distinct thermoelectric performance. The Fig. 7(e) for lattice thermal conductivity demonstrates that both materials experience a significant increase in κ_l as temperature rises from 50 K to generally 300 K. Although κ_l begins to saturate, especially with Bi_2PbSe_4 . This thermal saturation indicates that phonon–phonon Umklapp scattering takes priority at high temperatures. Between 300 K and 650 K, Bi_2PbSe_4 shows a higher and flatter κ_l profile ($7.5\text{--}7.8 \times 10^{14} \text{ W m}^{-1} \text{ K}^{-1} \text{ s}^{-1}$), showing steady phonon transport in that range. Bi_2PbTe_4 has a slightly greater value κ_l at 50 K ($2.58 \times 10^{14} \text{ W m}^{-1} \text{ K}^{-1} \text{ s}^{-1}$), but rises slowly and consistently below Bi_2PbSe_4 after 150 K, attaining $7.31 \times 10^{14} \text{ W m}^{-1} \text{ K}^{-1} \text{ s}^{-1}$ at 650 K. Te's higher atomic mass and phonon scattering decrease lattice

conductivity, which makes it ideal for thermoelectric materials with low κ_l and improved zT . Yet, the power factor (PF) curves (see Fig. 7(f)) favor Bi_2PbSe_4 . Its PF rises fast and linearly with temperature, starting at $8.77 \times 10^{11} \text{ W m}^{-1} \text{ K}^{-2} \text{ s}^{-1}$ at 50 K and reaching $6.67 \times 10^{11} \text{ W m}^{-1} \text{ K}^{-2} \text{ s}^{-1}$ at 650 K. This pattern shows a substantial increase in both Seebeck coefficient and electrical conductivity as temperature rises, suggesting optimal thermoelectric performance. Bi_2PbTe_4 , on the other hand, displays an increasing PF with temperature, though at a consistently lower magnitude, starting at $1.41 \times 10^{11} \text{ W m}^{-1} \text{ K}^{-2} \text{ s}^{-1}$ at 50 K and declining at $4.49 \times 10^{11} \text{ W m}^{-1} \text{ K}^{-2} \text{ s}^{-1}$ at 650 K. At low temperatures, it has a slightly greater PF due to superior electrical conductivity, but it rapidly loses position to Bi_2PbSe_4 at and above 100 K. Bi_2PbSe_4 's Seebeck coefficient increases with temperature without losing electrical conductivity, but Bi_2PbTe_4 loses this balance. Bi_2PbSe_4 possesses better electrical transport performance (PF) and greater κ_l . Bi_2PbTe_4 has lower lattice thermal conductivity, which is helpful for thermal performance. Yet its power factor performance is insufficient, limiting its efficiency. Bi_2PbTe_4 may benefit from lower phonon heat conduction, although Bi_2PbSe_4 is more attractive thermoelectrically because of its superior electronic performance.



4. Conclusions

This study examined the optoelectronic and thermoelectric properties of novel Bi_2PbSe_4 and Bi_2PbTe_4 with trigonal structure and space group $R\bar{3}m$, employing density functional theory. The minima's position along the volume axis effectively replicates the two materials' varying structural features, highlighting the equilibrium volume difference between them. Bi-p orbitals were substantially hybridized with p states of Se and Te in the valence band. Bi_2PbSe_4 and Bi_2PbTe_4 exhibit direct band gaps at (Γ - Γ) points, with predicted energy gaps of 1.12 and 0.71 eV for Bi_2PbSe_4 and 1.08 and 0.82 eV for Bi_2PbTe_4 using the TB-mBJ and PBE-GGA, respectively. Bi_2PbTe_4 has weak bonding due to Te larger size and its greater polarizability, leading to a smaller band gap. Because of their massive atomic number, bismuth atoms contributed significantly to the valence band, resulting in relativistic effects that caused considerable splitting of energy levels, resulting in the stabilization of Bi-p states. Bi_2PbTe_4 possesses stronger Bi-Pb interactions and lower Pb-chalcogen covalency than Bi_2PbSe_4 , which can be due to Te's larger size and polarizability. The peaks in $\varepsilon_1(\omega)$ signify resonances induced by electrical transitions between bands. Bi_2PbTe_4 had a higher $\varepsilon_1(0)$ value, signifying stronger polarizability and lower interband transition energy compared to Bi_2PbSe_4 . The peaks in $\varepsilon_2(\omega)$ corresponded to a substantial density of states, where interband transitions probably occurred. Bi_2PbTe_4 decreases to lower energy, revealing a denser and more accessible conduction band structure than Bi_2PbSe_4 . The heavier Te atom improved spin-orbit coupling and polarizability in Bi_2PbTe_4 , leading to an increased static refractive index. Bi_2PbSe_4 and Bi_2PbTe_4 exhibit $R(0)$ values of 0.35 and 0.40, indicating the material's natural ability to reflect light in the low-energy region. The $L(\omega)$, notably its peaks and subsequent decline, was significantly connected to optical properties and collective excitations in these materials. The dielectric function $\varepsilon(\omega)$ becomes less sensitive at higher frequencies because of electrons' inability to adapt to the rapidly fluctuating field, leading to a fall in $L(\omega)$. Bi_2PbTe_4 has a higher primary Seebeck coefficient of around 50 K than Bi_2PbSe_4 due to differences in band topologies, carrier effective masses, and intrinsic doping levels. The negative values of the Seebeck coefficients demonstrated that electrons were the primary charge carriers in both Bi_2PbSe_4 and Bi_2PbTe_4 . The reduction in electrical conductivity with higher temperatures in Bi_2PbSe_4 and Bi_2PbTe_4 can be explained by the combination of carrier concentration, mobility, and scattering. Variations and trends in zT values occurred when thermoelectric properties changed with temperature.

Conflicts of interest

There are no conflicts to declare.

Data availability

Data are available upon request from the corresponding author.

Acknowledgements

This work was supported and funded by the Deanship of Scientific Research at Imam Mohammad Ibn Saud Islamic University (IMSIU) (grant number IMSIU-DDRSP2503).

References

- 1 E. Hua, B. A. Engel, J. Guan, J. Yin, N. Wu, X. Han, S. Sun, J. He and Y. Wang, *Energy Convers. Manage.*, 2022, **266**, 115848.
- 2 K. Mokurala and S. Mallick, *RSC Adv.*, 2017, **7**, 18892.
- 3 A. Ghosh, A. Biswas, R. Thangavel and G. Udayabhanu, *RSC Adv.*, 2016, **6**, 96025–96034.
- 4 H. Khalifa, S. A. El-Safty, A. Reda, M. M. Selim and M. A. Shenashen, *Energy Storage Mater.*, 2021, **37**, 363–377.
- 5 L. Micheli, F. Almonacid, J. G. Bessa, Á. Fernández-Solas and E. F. Fernández, *Sustain. Energy Technol. Assess.*, 2024, **62**, 103607.
- 6 F. Khmaissia, H. Frigui, M. Sunkara, J. Jasinski, A. M. Garcia, T. Pace and M. Menon, *Comput. Mater. Sci.*, 2018, **147**, 304–315.
- 7 X.-Y. Tian, C.-X. Du, G. Zhao, R. M. SheLe, Y. Bao and M. Baiyin, *RSC Adv.*, 2020, **10**, 34903–34909.
- 8 M.-F. Wang, S.-M. Jang, J.-C. Huang and C.-S. Lee, *J. Solid State Chem.*, 2009, **182**, 1450–1456.
- 9 J.-Y. Park, J. H. Noh, T. N. Mandal, S. H. Im, Y. Jun and S. I. Seok, *RSC Adv.*, 2013, **3**, 24918.
- 10 P. Mangelis, A. Aziz, I. da Silva, R. Grau-Crespo, P. Vaquero and A. V. Powell, *Phys. Chem. Chem. Phys.*, 2019, **21**, 19311–19317.
- 11 J. Ji, Q. Gu, R. Khenata, F. Guo, Y. Wang, T. Yang and X. Tan, *RSC Adv.*, 2020, **10**, 39731–39738.
- 12 S. Mishra, P. Lohia and D. K. Dwivedi, *Phys. B*, 2019, **572**, 81–87.
- 13 Z. Aslam, A. Rashid Lone, M. Shoab and M. Zulfequar, *Chem. Phys. Lett.*, 2023, **814**, 140321.
- 14 S. Liu, W. Chen, C. Liu, B. Wang and H. Yin, *Results Phys.*, 2021, **26**, 104398.
- 15 E. Djatoubai and J. Su, *Chem. Phys. Lett.*, 2021, **770**, 138406.
- 16 M. Bouchenafa, A. Benmakhlof, M. Sidoumou, A. Bouhemadou, S. Maabed, M. Halit, A. Bentabet, S. Bin-Omran, R. Khenata and Y. Al-Douri, *Mater. Sci. Semicond. Process.*, 2020, **114**, 105085.
- 17 M. Cao, B. L. Zhang, J. Huang, Y. Sun, L. J. Wang and Y. Shen, *Chem. Phys. Lett.*, 2014, **604**, 15–21.
- 18 J. M. Fernández and A. M. Abietar, *Procedia Comput. Sci.*, 2011, **7**, 231–232.
- 19 J. Shi, T. F. Cerqueira, W. Cui, F. Nogueira, S. Botti and M. A. Marques, *Sci. Rep.*, 2017, **7**, 43179.
- 20 G. Yang, L. Sang, F. F. Yun, D. R. Mitchell, G. Casillas, N. Ye, K. See, J. Pei, X. Wang, J. Li, G. J. Snyder and X. Wang, *Adv. Funct. Mater.*, 2021, **31**, 2008851.
- 21 M. G. Voss, J. R. Challa, D. T. Scholes, P. Y. Yee, E. C. Wu, X. Liu, S. J. Park, O. León Ruiz, S. Subramanian, M. Chen, S. A. Jenekhe, X. Wang, S. H. Tolbert and B. J. Schwartz, *Adv. Mater.*, 2020, **33**, 2000228.



- 22 X.-L. Shi, J. Zou and Z.-G. Chen, *Chem. Rev.*, 2020, **120**, 7399–7515.
- 23 S. Wang, Y. Xiao, Y. Chen, S. Peng, D. Wang, T. Hong, Z. Yang, Y. Sun, X. Gao and L.-D. Zhao, *Energy Environ. Sci.*, 2021, **14**, 451–461.
- 24 B. Jiang, Y. Yu, J. Cui, X. Liu, L. Xie, J. Liao, Q. Zhang, Y. Huang, S. Ning, B. Jia, B. Zhu, S. Bai, L. Chen, S. J. Pennycook and J. He, *Science*, 2021, **371**, 830–834.
- 25 Y. Gan, Y. Huang, N. Miao, J. Zhou and Z. Sun, *J. Mater. Chem. C*, 2021, **9**, 4189–4199.
- 26 F. Cai, R. Dong, W. Sun, X. Lei, B. Yu, J. Chen, L. Yuan, C. Wang and Q. Zhang, *Chem. Mater.*, 2021, **33**, 6003–6011.
- 27 N. K. Singh and A. Soni, *Appl. Phys. Lett.*, 2020, **117**, 123901.
- 28 T. Schröder, M. N. Schneider, T. Rosenthal, A. Eisele, C. Gold, E.-W. Scheidt, W. Scherer, R. Berthold and O. Oeckler, *Phys. Rev. B*, 2011, **84**, 184104.
- 29 S. Glasco, *French Rev.*, 2012, **85**, 1222–1223.
- 30 P. P. Konstantinov, L. E. Shelimova, E. S. Avilov, M. A. Kretova and J.-P. Fleurial, *J. Solid State Chem.*, 1999, **146**, 305–312.
- 31 S. Bagci, B. G. Yalcin, H. A. R. Aliabad, S. Duman and B. Salmankurt, *RSC Adv.*, 2016, **6**, 59527–59540.
- 32 G. M. Stephen, O. A. Vail, J. Lu, W. A. Beck, P. J. Taylor and A. L. Friedman, *Sci. Rep.*, 2020, **10**, 4845.
- 33 R. J. Cava, H. Ji, M. K. Fuccillo, Q. D. Gibson and Y. S. Hor, *J. Mater. Chem. C*, 2013, **1**, 3176.
- 34 L. Tan, Y. Zhang, Y. Chen and Y. Chen, *Chem. Phys. Lett.*, 2015, **622**, 1–8.
- 35 J. Luitz, M. Maier, C. Hébert, P. Schattschneider, P. Blaha, K. Schwarz and B. Jouffrey, *Eur. Phys. J. B*, 2001, **21**, 363–367.
- 36 J. P. Perdew, K. Burke and M. Ernzerhof, *Phys. Rev. Lett.*, 1996, **77**, 3865–3868.
- 37 F. Tran, P. Blaha and K. Schwarz, *J. Phys.: Condens. Matter*, 2007, **19**, 196208.
- 38 P. Giannozzi, S. Baroni, N. Bonini, M. Calandra, R. Car, C. Cavazzoni and R. M. Wentzcovitch, *J. Phys.: Condens. Matter*, 2009, **21**, 395502.
- 39 G. K. H. Madsen and D. J. Singh, *Comput. Phys. Commun.*, 2006, **175**, 67–71.

